Unified Unsupervised Unmixing with Sparse Noise Estimation for Linear and Multilinear Models

Daniel Ulises Campos-Delgado[1], Juan Nicolás Mendoza-Chavarría[1], Omar Gutierrez-Navarro[2], Laura Quintana-Quintana[3], and Gustavo Callico[3]

***Abstract*—Multimodal images (MIs) can capture different modalities of a scene with multiple applications in medicine, remote sensing, food inspection, among others. Over a 2D domain, these images acquire spectral/morphological/temporal information of each spatial point. Unmixing methodologies can decompose this spatial and spectral/morphological/temporal information. In this letter, a unified framework is proposed for unsupervised unmixing, explicitly accounting for Gaussian and sparse noise. Our approach is novel in three key aspects: (i) addresses the general case of multimodal images, (ii) unifies linear and multilinear mixing models, and (iii) incorporates noise effects into the synthesis schemes. The proposed methodology relies on cyclic coordinate descent optimization (CCDO), constrained quadratic estimation, and L1-regularization. For the validation stage, two types of synthetic MIs were used with additive Gaussian and sparse noise terms. Additionally, the Urban dataset was employed for further validation to consider a real-world scenario. The results show that the proposed methodologies provide accurate reconstructions of the datasets, as well as the ground-truth abundance maps and end-members with low computational time.**

***Index Terms*—linear unmixing, multilinear unmixing, correlated multimodal images, sparse noise**

I. INTRODUCTION

DIGITAL imaging is a powerful tool for automatic inspection and evaluation of a given scene. An evolution of this tool is given by MIs [1], where different modalities of the scene are captured, for example (i) spatial and spectral (hyperspectral imaging, HSI) [2], and (ii) spatial and spectral/temporal (multi-spectral fluorescence lifetime imaging microscopy, m-FLIM) [3]. After data acquisition of a MI, the next challenge is to perform a proper and efficient analysis of the captured information. Unmixing methodologies can help to analyze and decompose the spectral, morphological or temporal responses from the spatial information: end-members and their abundances [4], [5]. The end-members represent basic spectral/temporal/morphological responses which are common in the 3D tensor; and the abundances stand for their spatial contributions over the 2D domain. Furthermore, the relationship between end-members and their abundances can be represented by linear and nonlinear mixing models (LMM and NMM) [6], [7]. In HSI, nonlinear mixing models have also been suggested to physically represent multiple-scattering effects during the optical acquisition process [8]. In this sense, the multilinear mixing model (MMM) is a relevant representation [9], where at each spatial point, a scalar parameter quantifies the nonlinear optical interactions. In fact, recent contributions with LMM and MMM also consider deep-learning strategies for unsupervised unmixing, where deep autoencoders networks were implemented by using fully-connected or convolutional networks [10], [11].

During the acquisition process of MIs, noise could be induced by instrumentation and environmental effects: thermal (Johnson), quantization, strip and shot (photon) [12], which could mislead and disrupt the unmixing process. While preprocessing could attenuate the noise negative effects, aggressive denoising might remove valuable spectral information, potentially distorting the unmixing results [13]. With a supervised perspective, linear unmixing was addressed with Gaussian and sparse noise components in [14], where total-variation-based regularization, sparsity constraints, and split-Bregman method were used to derive an iterative optimization scheme. Meanwhile, in [13], also with a supervised perspective, linear unmixing was studied considering Gaussian, sparse, and strip noise components, and a self-adjusted stepsize was proposed during the iterative optimization algorithms. In this context, this letter introduces a unified framework for treating linear and nonlinear unmixing schemes for MIs with an unsupervised perspective by considering Gaussian and sparse noise sources in their synthesis schemes, while keeping closed-form solutions and guaranteeing convergence. This technical contribution departs from our previous unmixing strategies: extended blind end-member and abundance extraction (EBEAE) [15], and nonlinear EBEAE (NEBEAE) [16], where an initial version of this contribution was presented in [17].

The notation used in this work is described below. Scalars, vectors, matrices and tensors are denoted by italic, boldface lowercase, boldface uppercase and underlined-boldface uppercase letters, respectively. An L-dimensional vector with unitary entries and the corresponding identity matrix are defined as $\mathbf{1}_L$, and $\mathbf{I}_L$, respectively. For a general vector $\mathbf{x}$, its transpose is represented by $\mathbf{x}^\top$, its l-th component by $(\mathbf{x})_l$, its Euclidean norm by $\|\mathbf{x}\| = \sqrt{\sum_l (\mathbf{x})_l^2}$, the L_1 norm by $\|\mathbf{x}\|_1 = \sum_l |\mathbf{x}_l|$, and $|\mathbf{x}|$ represents a new vector obtained by applying the absolute value component-wise. For two vectors

This work was supported by Ministerio de Universidades with a Maria Zambrano fellowship ING-ARQ/6431200-(SI-1821); Spanish Government and European Union (FEDER funds) as part of (i) TALENT-HExPERIA project ref. PID2020-116417 RB-C42, and (ii) OASIS project ref. PID2023-148285OB-C43; and CONAHCYT by a doctoral fellowship (#865747).

1 College of Science, Universidad Autonoma de San Luis Potosi, SLP, Mexico (e-mail: ducd@fciencias.uaslp.mx, a191603@alumnos.uaslp.mx)

[2] Biomedical Engineering Department, Universidad Autonoma de Aguascalientes, AGS, Mexico (e-mail: omar.gutierrezn@edu.uaa.mx)

[3] Institute for Applied Microelectronics, University of Las Palmas de Gran Canaria, Las Palmas de Gran Canaria, Spain (e-mail: lquintana@iuma.ulpgc.es, gustavo@iuma.ulpgc.es)

$\mathbf{x}$ and $\mathbf{y}$, $\mathbf{x} \odot \mathbf{y}$ defines its Hadamard product. For a matrix $\mathbf{X}$, $\|\mathbf{X}\|_F = \sqrt{\mathrm{Tr}(\mathbf{X}\mathbf{X}^\top)}$ denotes its Frobenius norm, where $\mathrm{Tr}(\cdot)$ expresses the trace operation. A diagonal matrix formed by the elements in $\mathbf{x}$ is defined as $\mathrm{diag}(\mathbf{x})$, and for a symmetric matrix $\mathbf{X}$, $\lambda_{min}(\mathbf{X})$ represents its minimum eigenvalue. For a set $\mathcal{X}$, $\mathrm{card}(\mathcal{X})$ denotes its cardinality.

II. Methodology

A. Unmixing problem formulation

We assume a MI represented by a 3D tensor $\underline{\mathbf{X}} \in \mathbb{R}^{L\times N_x \times N_y}$ where each element is considered non-negative, L is the number of samples in the spectral, time or morphological domain, and N_x and N_y are the spatial dimensions. The tensor $\underline{\mathbf{X}}$ is reshaped by unfolding the spatial domain into a 2D matrix $\mathbf{Z} \in \mathbb{R}^{L\times K}$ where $K = N_x \times N_y$. In this way, each column $\mathbf{z}_k \in \mathbb{R}^L$ of $\mathbf{Z}$ represents the spectral/morphological/time response of a spatial point, with $\mathbf{z}_k \geq 0$ component-wise for all $k \in \mathcal{K} = \{1,\dots,K\}$. Following previous works [15], [16], these measurements are scaled to sum-to-one to avoid numerical problems $\mathbf{y}_k = \mathbf{z}_k/(\mathbf{1}_L^\top \mathbf{z}_k)$ $\forall k \in \mathcal{K}$. In this way, the set of original and scaled measurements are defined as $\mathcal{Z} = \{\mathbf{z}_1,\dots,\mathbf{z}_K\}$ and $\mathcal{Y} = \{\mathbf{y}_1,\dots,\mathbf{y}_K\}$, respectively. In what follows, we will present the corresponding equations for linear and multilinear models associated with each variable or optimization term within a unified framework [15], [16]. Hence, the k-th scaled measurement is represented by a N-th order mixing model:

$$\mathbf{y}_k = \begin{cases} \mathbf{P}\boldsymbol{\alpha}_k + \mathbf{n}_k + \mathbf{v}_k, & \text{(LMM)} \\ (1-d_k)\mathbf{P}\boldsymbol{\alpha}_k + d_k(\mathbf{P}\boldsymbol{\alpha}_k)\odot \mathbf{z}_k + \mathbf{n}_k + \mathbf{v}_k, & \text{(MMM)} \end{cases} \tag{1}$$

where $\mathbf{P} = [\mathbf{p}_1 \dots \mathbf{p}_N] \in \mathbb{R}^{L\times N}$ is the matrix of end-members, $\mathbf{p}_n \in \mathbb{R}^L$ is the n-th end-member ($\mathbf{p}_n \geq 0$) $\forall n \in \mathcal{N} = \{1,\dots,N\}$, $\boldsymbol{\alpha}_k = [\alpha_{k,1}\dots\alpha_{k,N}]^\top \in \mathbb{R}^N$ is the vector of abundances at k-th measurement, $\alpha_{k,n} \geq 0$ denotes the abundance of n-th end-member, $d_k \in (-\infty, 1]$ is the nonlinear interaction level in a MMM, $\mathbf{n}_k \in \mathbb{R}^L$ represents sparse noise, and $\mathbf{v}_k \in \mathbb{R}^L$ is a white noise vector. The elements in $\mathbf{v}_k$ are assumed zero-mean and i.i.d. with a Gaussian distribution ($\mathbf{1}_L^\top \mathbf{v}_k \approx 0$), and the set of end-members $\mathcal{P} = \{\mathbf{p}_1,\dots,\mathbf{p}_N\}$ is linearly independent. As shown in [16], due to the normalization condition on the scaled measurements $\mathbf{1}_L^\top \mathbf{y}_k = 1$ $\forall k \in \mathcal{K}$, the following restrictions are imposed:

$$\mathbf{1}_L^\top \mathbf{p}_n = 1.0 \quad \& \quad \mathbf{p}_n \geq 0, \tag{2}$$

$$\boldsymbol{\delta}_k^\top \boldsymbol{\alpha}_k + \mathbf{1}_L^\top \mathbf{n}_k = 1.0 \quad \& \quad \boldsymbol{\alpha}_k \geq 0, \tag{3}$$

where $\boldsymbol{\delta}_k \in \mathbb{R}^N$ is adjusted according to the mixing model:

$$\boldsymbol{\delta}_k = \begin{cases} \mathbf{1}_N, & \text{(LMM)} \\ (1-d_k)\mathbf{1}_N + d_k \mathbf{P}^\top \mathbf{z}_k, & \text{(MMM)} \end{cases}. \tag{4}$$

In this framework, EBEAE and NEBEAE with sparse noise (EBEAE-SN & NEBEAE-SN) synthesis problems are formulated as CCDO schemes, where the cost functions include four key elements: (i) Reconstruction error term (RET), (ii) abundances entropy component, (iii) sparse noise regularization, and (iv) end-members similarity term [15], [16]:

$$\min \frac{1}{2K}\mathrm{RET} - \frac{\mu}{2K}\sum_{k\in\mathcal{K}} \|\boldsymbol{\alpha}_k\|^2 + \frac{\lambda}{K}\sum_{k\in\mathcal{K}}\|\mathbf{n}_k\|_1 + \frac{\rho}{2\vartheta}\sum_{n=1}^{N-1}\sum_{j=n+1}^{N}\|\mathbf{p}_n - \mathbf{p}_j\|^2, \tag{5}$$

such that (2) and (3) are jointly satisfied and

$$\mathrm{RET} = \begin{cases} \sum_{k\in\mathcal{K}} \frac{\|\mathbf{y}_k - \mathbf{P}\boldsymbol{\alpha}_k - \mathbf{n}_k\|^2}{\|\mathbf{y}_k\|^2}, & \text{(LMM)} \\ \sum_{k\in\mathcal{K}} \frac{\|\mathbf{y}_k - (1-d_k)\mathbf{P}\boldsymbol{\alpha}_k - d_k(\mathbf{P}\boldsymbol{\alpha}_k)\odot\mathbf{z}_k - \mathbf{n}_k\|^2}{\|\mathbf{y}_k\|^2}, & \text{(MMM)} \end{cases} \tag{6}$$

where $\vartheta = (N-1)+\dots+1$ for $N \geq 3$ and $\vartheta = 1$ for $N = 2$. For EBEAE-SN, the optimization variables in (5) are $\mathbf{P}$, $\{\boldsymbol{\alpha}_k\}$ and $\{\mathbf{n}_k\}$, and for NEBEAE-SN, it also includes $\{d_k\}$. Since a CCDO is applied to solve iteratively (5), at a time, one type of variable is optimized and the rest are kept fixed. The unified proposed algorithm is described in Algorithm 1, and the solutions to the individual optimization problem are briefly described next.

B. Abundance estimation

The cost function in (5) is written just with respect to the abundance vector $\boldsymbol{\alpha}_k$ at the k-th spatial location:

$$\min_{\boldsymbol{\alpha}_k \geq 0,\ \boldsymbol{\delta}_k^\top\boldsymbol{\alpha}_k = 1-\mathbf{1}_L^\top\mathbf{n}_k} \frac{1}{2}\frac{\|\mathbf{s}_k - \boldsymbol{\Lambda}_k\boldsymbol{\alpha}_k\|^2}{\|\mathbf{y}_k\|^2} - \frac{\mu}{2}\|\boldsymbol{\alpha}_k\|^2, \tag{7}$$

where $\mathbf{s}_k = \mathbf{y}_k - \mathbf{n}_k$, and

$$\boldsymbol{\Lambda}_k = \begin{cases} \mathbf{P}, & \text{(LMM)} \\ \mathbf{P}\odot\left[(1-d_k)\mathbf{1}_{L\times N} + d_k \mathbf{z}_k^\top \mathbf{1}_N\right]. & \text{(MMM)} \end{cases} \tag{8}$$

Following a similar derivation as in [15], the hyper-parameter μ in (7) is redefined as $\mu = \tilde{\mu}\cdot\lambda_{min}(\boldsymbol{\Lambda}_k^\top\boldsymbol{\Lambda}_k)/\|\mathbf{y}_k\|^2$ where $\tilde{\mu} \in [0,1)$ is a new normalized hyper-parameter. The solution to the constrained quadratic optimization in (7) is:

$$\boldsymbol{\alpha}_k = \boldsymbol{\Theta}_k \cdot \left(\boldsymbol{\Lambda}_k^\top \mathbf{s}_k - \frac{\mathbf{s}_k^\top\boldsymbol{\Lambda}_k\boldsymbol{\Theta}_k\boldsymbol{\delta}_k - \left[1 - \mathbf{1}_L^\top\mathbf{n}_k\right]}{\boldsymbol{\delta}_k^\top\boldsymbol{\Theta}_k\boldsymbol{\delta}_k}\mathbf{1}_N\right), \tag{9}$$

where $\boldsymbol{\Theta}_k = \left(\boldsymbol{\Lambda}_k^\top\boldsymbol{\Lambda}_k - \tilde{\mu}\lambda_{min}(\boldsymbol{\Lambda}_k^\top\boldsymbol{\Lambda}_k)\mathbf{I}_N\right)^{-1}$.

C. Sparse noise estimation

From (5), for the k-th measurement, the sparse noise term $\mathbf{n}_k$ is estimated by the following problem:

$$\min_{\mathbf{n}_k \geq 0} \|\mathbf{n}_k\|_1 + \frac{1}{2\lambda}\frac{\|\mathbf{n}_k - \mathbf{e}_k\|^2}{\|\mathbf{y}_k\|^2}, \tag{10}$$

where

$$\mathbf{e}_k = \begin{cases} \mathbf{y}_k - \mathbf{P}\boldsymbol{\alpha}_k, & \text{(LMM)} \\ \mathbf{y}_k - (1-d_k)\mathbf{P}\boldsymbol{\alpha}_k - d_k(\mathbf{P}\boldsymbol{\alpha}_k)\odot\mathbf{z}_k. & \text{(MMM)} \end{cases} \tag{11}$$

Since this optimization involves a L_1-regularized problem, a solution is reached by a shrinkage operation [18]:

$$\mathbf{n}_k = \mathrm{sign}(\mathbf{e}_k)\odot\max\left\{0, |\mathbf{e}_k| - \lambda\|\mathbf{y}_k\|^2\right\}. \tag{12}$$

where $\mathrm{sign}(\cdot)$ is applied component-wise. Finally, a rectifier unit is applied to the estimation $\mathbf{n}_k$ to guarantee positive entries $\forall k$. By analyzing the solution in (12), there is no coupling among all spatial points, so a matrix computation can be pursued to obtain in parallel the estimation process:

$$\mathbf{N} = \mathrm{sign}(\mathbf{E})\odot\max\left(\mathbf{0}, |\mathbf{E}| - \lambda\mathbf{Y}_e\right), \tag{13}$$

where $\mathbf{N} = [\mathbf{n}_1\dots\mathbf{n}_K]$, $\mathbf{E} = [\mathbf{e}_1\dots\mathbf{e}_K]$, and $\mathbf{Y}_e = \left[\|\mathbf{y}_1\|^2\cdot\mathbf{1}_L \ \dots\ \|\mathbf{y}_K\|^2\cdot\mathbf{1}_L\right]$.

This article has been accepted for publication in IEEE Signal Processing Letters. This is the author's version which has not been fully edited and content may change prior to final publication. Citation information: DOI 10.1109/LSP.2025.3582539

D. End-members estimation

The cost-function in (5) is written with respect to the end-members matrix $\mathbf{P}$:

$$\min_{\mathbf{p}_n\geq 0,\mathbf{1}_L^\top\mathbf{p}_n=1}\frac{1}{2K}\text{EMET}+\frac{\rho}{2\vartheta}\sum_{n=1}^{N-1}\sum_{j=n+1}^{N}\|\mathbf{p}_n-\mathbf{p}_j\|^2, \quad (14)$$

where

$$\text{EMET}=\begin{cases}\sum_{k\in\mathcal{K}}\frac{\|\mathbf{s}_k-\mathbf{P}\boldsymbol{\alpha}_k\|^2}{\|\mathbf{y}_k\|^2}, & \text{(LMM)}\\ \sum_{k\in\mathcal{K}}\frac{\|\mathbf{s}_k-(1-d_k)\mathbf{P}\boldsymbol{\alpha}_k-d_k(\mathbf{P}\boldsymbol{\alpha}_k)\odot\mathbf{z}_k\|^2}{\|\mathbf{y}_k\|^2}. & \text{(MMM)}\end{cases} \quad (15)$$

For the LMM, the constrained optimization problem is quadratic and admits a closed-solution by following a similar derivation as in [19]:

$$\mathbf{P}=\left(\mathbf{I}_L-\frac{\mathbf{1}_L\mathbf{1}_L^\top}{L}\right)\mathbf{SWA}^\top\left(\mathbf{AWA}^\top+\frac{\rho}{\vartheta}\mathbf{O}\right)^{-1}+\frac{\mathbf{1}_L\mathbf{1}_N^\top}{L}, \quad (16)$$

where $\mathbf{S}=\mathbf{Y}-\mathbf{N}$, $\mathbf{Y}=[\mathbf{y}_1\ldots\mathbf{y}_K]$, $\mathbf{A}=[\boldsymbol{\alpha}_1\ldots\boldsymbol{\alpha}_K]$, $\mathbf{W}=(1/K)\text{diag}([1/\|\mathbf{y}_1\|^2\ \ldots\ 1/\|\mathbf{y}_K\|^2])$ and $\mathbf{O}=N\mathbf{I}_N-\mathbf{1}_N\mathbf{1}_N^\top$. Meanwhile, for the MMM, a closed-solution is not viable, so an iterative gradient descent approach with an optimized linear search is considered (as in [16]), so at the l-th iteration, the update is:

$$\mathbf{P}^{l+1}=\mathbf{P}^l-\gamma^l\boldsymbol{\Gamma}^l \qquad l\geq 0, \quad (17)$$

where

$$\boldsymbol{\Gamma}^l=\sum_{k\in\mathcal{K}}\left\{\frac{-(\mathbf{M}_k^l)^\top\mathbf{s}_k^l(\boldsymbol{\alpha}_k^l)^\top}{K\|\mathbf{y}_k\|^2}+\frac{(\mathbf{M}_k^l)^\top\mathbf{M}_k^l\mathbf{P}^l\boldsymbol{\alpha}_k^l(\boldsymbol{\alpha}_k^l)^\top}{K\|\mathbf{y}_k\|^2}\right\}+\frac{\rho\mathbf{P}^l\mathbf{O}}{2\vartheta}, \quad (18)$$

$\mathbf{M}_k^l=(1-d_k^l)\mathbf{I}_L-d_k^l\text{diag}(\mathbf{z}_k)$, and $\gamma^l=\max\left(0,\frac{\gamma_{num}^l}{\gamma_{den}^l}\right)$, such that:

$$\gamma_{num}^l=\sum_{k\in\mathcal{K}}\frac{(\boldsymbol{\alpha}_k^l)^\top(\boldsymbol{\Gamma}^l)^\top(\mathbf{M}_k^l)^\top(\mathbf{M}_k^l)(\mathbf{P}^l\boldsymbol{\alpha}_k^l-\mathbf{s}_k^l)}{K\|\mathbf{y}_k\|^2}+\rho\,\text{Tr}\left(\boldsymbol{\Gamma}^l\mathbf{O}(\mathbf{P}^l)^\top+\mathbf{P}^l\mathbf{O}(\boldsymbol{\Gamma}^l)^\top\right)/2\vartheta, \quad (19)$$

$$\gamma_{den}^l=\sum_{k\in\mathcal{K}}\frac{(\boldsymbol{\alpha}_k^l)^\top(\boldsymbol{\Gamma}^l)^\top(\mathbf{M}_k^l)^\top\mathbf{M}_k^l\boldsymbol{\Gamma}^l\boldsymbol{\alpha}_k^l}{K\|\mathbf{y}_k\|^2}+\frac{\rho\text{Tr}\left(\boldsymbol{\Gamma}^l\mathbf{O}(\boldsymbol{\Gamma}^l)^\top\right)}{\vartheta}. \quad (20)$$

E. Estimation of Nonlinear Interaction Level

Finally, for the MMM, the resulting quadratic problem in (5) for the k-th nonlinear interaction level d_k is given by:

$$\min_{d_k\in(-\infty,1]}\frac{1}{2}\frac{\|\mathbf{q}_k+d_k\mathbf{m}_k\|^2}{\|\mathbf{y}_k\|^2}\quad\forall k\in\mathcal{K}. \quad (21)$$

where $\mathbf{q}_k=\mathbf{y}_k-\mathbf{P}\boldsymbol{\alpha}_k-\mathbf{n}_k$, and $\mathbf{m}_k=\mathbf{P}\boldsymbol{\alpha}_k-(\mathbf{P}\boldsymbol{\alpha}_k)\odot\mathbf{z}_k$. As a result, the optimal solution is achieved as [16]:

$$d_k=\min\left(1,-\frac{\mathbf{q}_k^\top\mathbf{m}_k}{\|\mathbf{m}_k\|^2}\right). \quad (22)$$

F. Implementation of iterative optimization

In our proposals, there are four hyper-parameters $(N,\tilde{\mu},\lambda,\rho)$ that influence the unmixing process, i.e. order of the model, and weights on abundances entropy, sparse noise regularization, and end-members similarity, respectively [15], [16]. Meanwhile, the optimization problems in (7), (10), (14) and (21) are all convex and they allow closed-solutions, as shown in (9), (13), (16), and (21), respectively. The only exception is the end-member estimation for the MMM, which is solved iteratively by (17). Therefore, in the CCDO iteration, a convergent iteration is expected, and at l-th step, the global estimation error is computed by $J^l=\|\mathbf{Y}-\hat{\mathbf{Y}}^l\|_F$ where

$$\hat{\mathbf{Y}}^l=\begin{cases}\mathbf{P}^l\mathbf{A}^l+\mathbf{N}^l, & \text{(LMM)}\\ \boldsymbol{\Omega}^l\odot(\mathbf{P}^l\mathbf{A}^l)+\mathbf{D}^l\odot(\mathbf{P}^l\mathbf{A}^l)\odot\mathbf{Z}+\mathbf{N}^l, & \text{(MMM)}\end{cases} \quad (23)$$

$\boldsymbol{\Omega}^l=\mathbf{1}_{L\times N}-\mathbf{D}^l$, and $\mathbf{D}^l=\left[d_1^l\cdot\mathbf{1}_L\ \ldots\ d_K^l\cdot\mathbf{1}_L\right]$. With these definitions, we propose the convergence conditions:

$$\frac{|J^l-J^{l+1}|}{J^l}<\epsilon \quad\vee\quad l\geq l_{max}, \quad (24)$$

where $\epsilon>0$ is a minimum improvement threshold, and l_{max} the maximum iterations.

Algorithm 1 EBEAE-SN and NEBEAE-SN Methodologies

Input: Set of measurements $\mathcal{Z}$, hyper-parameters $(N,\tilde{\mu},\lambda,\rho)$, initial matrix $\mathbf{P}^0$, and convergence parameters ϵ and l_{max}.
Output: End-member matrix $\mathbf{P}$, abundances matrix $\mathbf{A}$, sparse noise matrix $\mathbf{N}$, estimated scaled measurements $\hat{\mathbf{Y}}$, and for MMM, $\{d_k\}$ nonlinear interaction levels.

```
1: Normalize measurements set Z to obtain Y.
2: Set l = 0, J^0 = 10^6, and assign abundances, sparse noise
   components, and for MMM, nonlinear interaction levels
   to zero, i.e. α_k^0 = 0, n_k^0 = 0, and d_k^0 = 0 ∀k ∈ K.
3: while Convergence condition in (24) is not satisfied. do
4:    Update abundances α_k^{l+1} by (9) ∀k ∈ K.
5:    Update N^{l+1} by (13).
6:    For LMM, update P^{l+1} by (16), and for MMM, by the
      gradient descent rule in (17).
7:    For MMM, update d_k^{l+1} by (22).
8:    Compute Ŷ^{l+1} by (23), update J^{l+1} and l ← l + 1.
9: end while
```

III. Validation results

To provide a common baseline for validation, synthetic MIs were used under two noise models: (i) Gaussian noise, controlled via a signal-to-noise ratio (SNR), and (ii) sparse uniformly distributed (SUD) noise, defined by a density level. Performance was assessed using the following metrics with respect to ground-truth (GT): (a) normalized error in measurements, (b) error in abundances, (c) error in end-members, (d) spectral angle mapper (SAM) for end-members, (e) computational time, and for the MMM, (f) normalized error in nonlinear interaction levels [16]. In addition, these synthetic MIs were used to analyze the convergence behavior of the proposed algorithms, and the results are presented in the *Supplementary Material*. To complement the synthetic experiments, the Urban hyperspectral dataset was included to evaluate the methods under real-world conditions [20], and this validation step is also included in the *Supplementary Material*. All MATLAB scripts are available at: https://github.com/Nicothe4th/EBEAE-SN.

For the LMM scenario, a m-FLIM synthetic MI with four fluorophores and three spectral bands is used [3]. The spatial dimension is 128×128 pixels with 558 time samples. The GT for abundances and end-members are shown in Fig. 1-a). The abundance maps were generated by a Gaussian mixture to show regions of high and low concentrations for each fluorophore. We compare EBEAE-SN with: (i) EBEAE [15], (ii) preserving intrinsic structure invariant non-negative matrix factorization (PISI-NMF) [21], (iii) hyperspectral unmixing with joint sparsity and total variation (HU-JSTV) [14], and (iv) dual simplex volume maximization for simplex-structured matrix factorization (Max-Vol-Dual) [22]. A Monte Carlo analysis with 50 realizations for each noise level was conducted. Table I shows a significant improvement in the measurements error by our proposal EBEAE-SN, outperforming the rest of the methods by an order of magnitude. In addition, this improvement is also shown for the metrics concerning abundances and end-member errors, and SAM in end-members with statistically significant differences. Finally, with respect to computational time, our proposal ranked second, just surpassed by EBEAE.

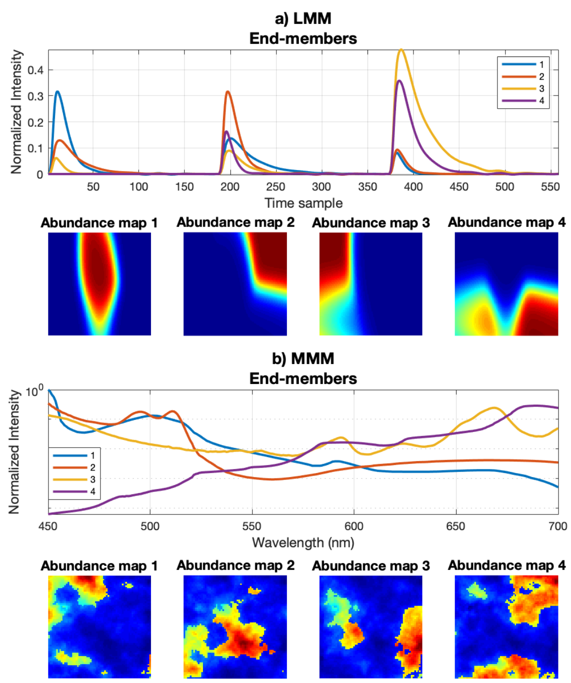

Fig. 1. Ground-truths of end-members & abundance maps for the synthetic MIs: (a) m-FLIM with LMM, and (b) HSI with MMM.

In the MMM scenario, a visible and near-infrared synthetic HSI was employed as a MI, whose dimensions are 64×64 pixels with 281 spectral bands. The GT for end-members and abundances are shown in Fig. 1-b). The end-members represent the absorbance of oxygenated and deoxygenated hemoglobin, fat and water [23]. Meanwhile, abundance maps were generated by the HYperspectral Data Retrieval and Analysis (HYDRA) toolbox with a spherical Gaussian pattern for N=4 components [24]. NEBEAE-SN was compared with four methodologies based on a MMM: (i) NEBEAE [16], (ii) a supervised approach for MMM [9] (SUP-MMM), (iii) an unsupervised scheme for MMM [25] (UNS-MMM), and (iv) a MMM unmixing based on particle swarm optimization [26] (AMMMPSO). The results of this validation stage are presented in Table II. Similar to the LMM analysis, a significant improvement was observed in the measurements error by NEBEAE-SN. Regarding errors in abundances, end-members, and nonlinear interaction levels, NEBEAE-SN did not show significant differences. Finally, in terms of computational time, NEBEAE outperformed the other methods, followed in two of the three cases by NEBEAE-SN.

TABLE I
MONTE CARLO RESULTS (MEAN $\pm$ STANDARD DEVIATION) OF SYNTHETIC LMM ANALYSIS (BOLD-FACE HIGHLIGHTS BEST PERFORMANCE).

SNR/ Density of SUD	EBEAE-SN (Proposed)	EBEAE	PISI-NMF	HU-JSTV	Max-Vol-Dual
Error in Measurements Estimation (%)					
30/0.01	**0.02 ± 0.0002**	0.29 ± 0.0004	0.29 ± 0.0048	0.3300 ± 0.62	0.31 ± 0.0011
35/0.0075	**0.01 ± 0.0002**	0.25 ± 0.0004	0.26 ± 0.0054	0.1800 ± 0.50	0.27 ± 0.0016
40/0.005	**0.01 ± 0.0002**	0.21 ± 0.0004	0.21 ± 0.0043	0.1500 ± 0.15	0.23 ± 0.0024
Error in Abundances Estimation					
30/0.01	**6.23 ± 0.4**	9.30 ± 0.9	8.92 ± 1.4	12.82 ± 7.0	13.56 ± 0.3
35/0.0075	**5.81 ± 0.8**	8.52 ± 0.9	8.39 ± 1.5	10.06 ± 5.2	14.09 ± 0.4
40/0.005	**5.47 ± 0.7**	7.40 ± 0.7	7.29 ± 1.2	12.72 ± 7.1	14.55 ± 0.6
Error in End-members Estimation ($\times 10^{-3}$)					
30/0.01	**3.13 ± 1.2**	6.55 ± 5.7	8.29 ± 1.2	8.66 ± 2.3	8.24 ± 0.4
35/0.0075	**2.96 ± 0.8**	5.18 ± 0.4	7.48 ± 0.1	7.11 ± 0.1	7.14 ± 0.5
40/0.005	**2.61 ± 0.4**	3.92 ± 0.3	5.59 ± 1.1	5.87 ± 1.6	6.18 ± 0.3
SAM in End-members Estimation ($\times 10^{-2}$)					
30/0.01	**2.15 ± 1.0**	3.65 ± 0.5	5.19 ± 0.9	5.60 ± 1.6	3.00 ± 0.03
35/0.0075	**1.95 ± 0.6**	2.96 ± 0.4	5.01 ± 1.2	4.82 ± 1.0	2.76 ± 0.02
40/0.005	**1.69 ± 0.3**	2.32 ± 0.3	3.96 ± 0.8	4.21 ± 1.1	2.27 ± 0.03
Computational Time (s)					
30/0.01	2.49 ± 0.8	**0.70 ± 0.1**	16.60 ± 1.0	14.88 ± 0.5	26.4 ± 7.9
35/0.0075	2.23 ± 0.4	**0.71 ± 0.1**	17.17 ± 1.1	15.17 ± 0.5	23.7 ± 1.4
40/0.005	2.23 ± 0.6	**0.74 ± 0.1**	16.40 ± 0.7	14.80 ± 0.4	23.6 ± 1.8

* No statistically significant difference (p-values > 0.05) compared to EBEAE-SN

TABLE II
MONTE CARLO RESULTS (MEAN $\pm$ STANDARD DEVIATION) OF SYNTHETIC MMM ANALYSIS (BOLD-FACE HIGHLIGHTS BEST PERFORMANCE).

SNR/ Density of SUD	NEBEAE-SN (Proposed)	NEBEAE	SUP-MMM	UNS-MMM	AMMMSPO
Error in Measurements Estimation (%)					
30/0.01	**0.02 ± 0.001**	0.59 ± 0.001	0.60 ± 0.002	0.59 ± 0.001	0.92 ± 0.002
35/0.0075	**0.02 ± 0.002**	0.54 ± 0.001	0.55 ± 0.002	0.54 ± 0.001	0.90 ± 0.002
40/0.005	**0.01 ± 0.001**	0.47 ± 0.001	0.48 ± 0.001	0.47 ± 0.001	0.90 ± 0.001
Error in Abundances Estimation					
30/0.01	**3.89 ± 1.7**	4.16 ± 0.4	6.24 ± 0.7	4.77 ± 1.0	6.18 ± 0.7
35/0.0075	**3.61 ± 1.5**	3.85 ± 0.6	6.00 ± 1.1	4.36 ± 0.5	6.12 ± 1.1
40/0.005	3.48 ± 0.8	**3.27 ± 0.5**$*$	5.90 ± 1.0	3.79 ± 0.5	5.78 ± 1.0
Error in End-members Estimation ($\times 10^{-2}$)					
30/0.01	1.45 ± 0.5	**1.33 ± 0.2**$*$	1.91 ± 0.4	$1.42 \pm 0.5*$	1.72 ± 0.4
35/0.0075	1.30 ± 0.3	$1.16 \pm 0.3*$	1.70 ± 0.5	**1.14 ± 0.2**$*$	1.76 ± 0.5
40/ 0.005	1.14 ± 0.3	**0.89 ± 0.3**$*$	1.54 ± 0.4	$0.94 \pm 0.2*$	1.51 ± 0.5
SAM in End-members Estimation ($\times 10^{-2}$)					
30/0.01	9.01 ± 3.3	**7.8 ± 1.5**$*$	12.88 ± 3.3	$9.5 \pm 3.3*$	11.5 ± 3.0
35/0.0075	8.03 ± 2.4	**6.8 ± 2.1**$*$	11.52 ± 3.9	$8.1 \pm 1.7*$	11.6 ± 3.4
40/0.005	7.24 ± 2.0	**5.4 ± 1.8**$*$	10.27 ± 3.4	$7.0 \pm 1.3*$	10.6 ± 3.0
Error in nonlinear Interaction Levels Estimation (%)					
30/0.01	0.30 ± 0.03	**0.27 ± 0.02**	0.45 ± 0.03	0.33 ± 0.02	1.15 ± 0.01
35/0.0075	0.22 ± 0.02	**0.20 ± 0.02**$*$	0.36 ± 0.02	0.26 ± 0.03	1.15 ± 0.01
40/0.005	0.15 ± 0.05	**0.13 ± 0.01**$*$	0.28 ± 0.02	0.19 ± 0.03	1.13 ± 0.01
Computational Time (s)					
30/0.01	6.37 ± 6.4	**2.27 ± 0.2**	6.03 ± 0.4*	6.97 ± 4.1	445.5 ± 9.64
35/0.0075	5.81 ± 5.5	**2.32 ± 0.3**	6.65 ± 0.4	7.36 ± 1.1	442.1 ± 3.21
40/0.005	5.09 ± 1.3	**2.23 ± 0.2**	7.08 ± 0.3	8.18 ± 0.5	440.9 ± 1.76

* No statistically significant difference (p-values > 0.05) compared to NEBEAE-SN

IV. CONCLUSIONS

This work presented a unified methodology extending our previous linear and multilinear unmixing strategies to handle both Gaussian and sparse noise components. Our results showed that EBEAE-SN and NEBEAE-SN outperformed other methods in synthetic MIs, with EBEAE-SN achieving the best abundance estimation, end-member error, and SAM. NEBEAE-SN offered the best balance between error metrics and computational time, showing no significant difference from the top methods. In the real-world scenario from remote sensing, our proposals excelled the comparison methods in the error metrics. However, despite performing an extra optimization step with the sparse noise matrix $\mathbf{N}$, both methods did not significantly increase computational time, achieving similar processing speeds to state-of-the-art methods.

References

[1] A. Walter et al., "Correlated multimodal imaging in life sciences: expanding the biomedical horizon," *Frontiers in Physics*, vol. 8, p. 47, 2020.

[2] A. Bhargava, A. Sachdeva, K. Sharma, M. H. Alsharif, P. Uthansakul, and M. Uthansakul, "Hyperspectral imaging and its applications: A review," *Heliyon*, vol. 10, no. 12, p. e33208, 2024.

[3] E. Duran-Sierra et al., "Clinical label-free biochemical and metabolic fluorescence lifetime endoscopic imaging of precancerous and cancerous oral lesions," *Oral Oncology*, vol. 105, p. 104635, 2020.

[4] J. M. Bioucas-Dias, A. Plaza, N. Dobigeon, M. Parente, Q. Du, P. Gader, and J. Chanussot, "Hyperspectral unmixing overview: Geometrical, statistical, and sparse regression-based approaches," *IEEE J. Sel. Top. Appl. Earth Obs. Remote Sens.*, vol. 5, no. 2, pp. 354–379, 2012.

[5] J. Chen, M. Zhao, X. Wang, C. Richard, and S. Rahardja, "Integration of physics-based and data-driven models for hyperspectral image unmixing: A summary of current methods," *IEEE Signal Processing Magazine*, vol. 40, no. 2, pp. 61–74, 2023.

[6] N. Dobigeon, Y. Altmann, N. Brun, and S. Moussaoui, "Chapter 6 - linear and nonlinear unmixing in hyperspectral imaging," in *Resolving Spectral Mixtures*, ser. Data Handling in Science and Technology, C. Ruckebusch, Ed. Elsevier, 2016, vol. 30, pp. 185–224.

[7] L. Drumetz, B. Ehsandoust, J. Chanussot, B. Rivet, M. Babaie-Zadeh, and C. Jutten, "Relationships between nonlinear and space-variant linear models in hyperspectral image unmixing," *IEEE Signal Processing Letters*, vol. 24, no. 10, pp. 1567–1571, 2017.

[8] R. Heylen, M. Parente, and P. Gader, "A review of nonlinear hyperspectral unmixing methods," *IEEE Journal of Selected Topics in Applied Earth Observations and Remote Sensing*, vol. 7, no. 6, pp. 1844–1868, 2014.

[9] R. Heylen and P. Scheunders, "A multilinear mixing model for nonlinear spectral unmixing," *IEEE Transactions on Geoscience and Remote Sensing*, vol. 54, no. 1, pp. 240–251, 2016.

[10] J. Chen, M. Zhao, X. Wang, C. Richard, and S. Rahardja, "Integration of physics-based and data-driven models for hyperspectral image unmixing: A summary of current methods," *IEEE Signal Processing Magazine*, vol. 40, no. 2, pp. 61–74, 2023.

[11] T. Fang, F. Zhu, and J. Chen, "Hyperspectral unmixing based on multilinear mixing model using convolutional autoencoders," *IEEE Transactions on Geoscience and Remote Sensing*, vol. 62, pp. 1–16, 2024.

[12] B. Rasti, P. Scheunders, P. Ghamisi, G. Licciardi, and J. Chanussot, "Noise reduction in hyperspectral imagery: Overview and application," *Remote Sensing*, vol. 10, no. 3, 2018.

[13] K. Naganuma and S. Ono, "Toward robust hyperspectral unmixing: Mixed noise modeling and image-domain regularization," *IEEE Journal of Selected Topics in Applied Earth Observations and Remote Sensing*, vol. 17, pp. 8117–8138, 2024.

[14] H. K. Aggarwal and A. Majumdar, "Hyperspectral unmixing in the presence of mixed noise using joint-sparsity and total variation," *IEEE Journal of Selected Topics in Applied Earth Observations and Remote Sensing*, vol. 9, no. 9, pp. 4257–4266, 2016.

[15] D. U. Campos-Delgado, O. Gutierrez-Navarro, J. J. Rico-Jimenez, E. Duran-Sierra, H. Fabelo, S. Ortega, G. Callico, and J. A. Jo, "Extended Blind End-Member and Abundance Extraction for Biomedical Imaging Applications," *IEEE Access*, vol. 7, pp. 178 539–178 552, 2019.

[16] D. U. Campos-Delgado, I. A. Cruz-Guerrero, J. N. Mendoza-Chavarría, A. R. Mejía-Rodríguez, S. Ortega, H. Fabelo, and G. M. Callico, "Nonlinear extended blind end-member and abundance extraction for hyperspectral images," *Signal Processing*, vol. 201, p. 108718, 2022.

[17] D. U. Campos-Delgado, J. N. Mendoza-Chavarria, J. A. Jo, R. Leon, H. Fabelo, and G. M. Callico, "Robust blind linear unmixing for correlated multimodal images in medical applications," in *2024 IEEE URUCON*, 2024, pp. 1–5.

[18] S. Boyd, N. Parikh, E. Chu, B. Peleato, and J. Eckstein, "Distributed optimization and statistical learning via the alternating direction method of multipliers," *Foundations and Trends in Machine Learning*, vol. 3, no. 1, pp. 1–122, 2011.

[19] O. Gutierrez-Navarro, D. U. Campos-Delgado, E. Arce-Santana, M. O. Mendez, and J. A. Jo, "Blind End-Member and Abundance Extraction for Multispectral Fluorescence Lifetime Imaging Microscopy Data," *IEEE J. Biomed. Heal. Informatics*, vol. 18, no. 2, pp. 606–617, 2014.

[20] F. Zhu, "Hyperspectral unmixing: Ground truth labeling, datasets, benchmark performances and survey," 2017. [Online]. Available: https://arxiv.org/abs/1708.05125

[21] Y. Shao, J. Lan, Y. Zhang, and J. Zou, "Spectral unmixing of hyperspectral remote sensing imagery via preserving the intrinsic structure invariant," *Sensors*, vol. 18, no. 10, 2018.

[22] M. Abdolali, G. Barbarino, and N. Gillis, "Dual simplex volume maximization for simplex-structured matrix factorization," *SIAM Journal on Imaging Sciences*, vol. 17, no. 4, pp. 2362–2391, 2024.

[23] S. Jacques and S. Prahl. Oregon medical laser center/ assorted spectra. [Online]. Available: https://omlc.org/spectra/index.html

[24] G. de Inteligencia Computacional-Universidad del País Vasco / Euskal Herriko Unibertsitatea (UPV/EHU)-Spain. Hyperspectral imagery synthesis (eias) toolbox. [Online]. Available: http://www.ehu.es/ccwintco/index.php/Hyperspectral_Imagery_Synthesis_tools_for_MATLAB

[25] Q. Wei, M. Chen, J.-Y. Tourneret, and S. Godsill, "Unsupervised nonlinear spectral unmixing based on a multilinear mixing model," *IEEE Transactions on Geoscience and Remote Sensing*, vol. 55, no. 8, pp. 4534–4544, 2017.

[26] B. Yang and Z. Yin, "Spectral variability augmented multi-linear mixing model for hyperspectral nonlinear unmixing," *IEEE Geoscience and Remote Sensing Letters*, vol. 21, pp. 1–5, 2024.